Research paper

On the effect of strain rate during the cyclic compressive loading of liquid crystal elastomers and their 3D printed lattices

Bo Song [a,*], Dylan Landry [a], Thomas Martinez [a], Christopher N. Chung [b], Kevin N. Long [a], Kai Yu [b], Christopher M. Yakacki [b]

[a] Sandia National Laboratories, Albuquerque, NM, 87123, USA
[b] Department of Mechanical Engineering, University of Colorado, Denver, CO, 80204, USA

ARTICLE INFO

ABSTRACT

Nematic liquid crystal elastomers (LCEs) are a unique class of network polymers with the potential for enhanced mechanical energy absorption and dissipation capacity over conventional network polymers because they exhibit both conventional viscoelastic behavior and soft-elastic behavior (nematic director changes under shear loading). This additional inelastic mechanism makes them appealing as candidate damping materials in a variety of applications from vibration to impact. The lattice structures made from the LCEs provide further mechanical energy absorption and dissipation capacity associated with packing out the porosity under compressive loading.

Understanding the extent of mechanical energy absorption, which is the work per unit mass (or volume) absorbed during loading, versus dissipation, which is the work per unit mass (or volume) dissipated during a loading cycle, requires measurement of both loading and unloading response. In this study, a bench-top linear actuator was employed to characterize the loading-unloading compressive response of polydomain and monodomain LCE polymers and polydomain LCE lattice structures with two different porosities (nominally, 62% and 85%) at both low and intermediate strain rates at room temperature. As a reference material, a bisphenol-A (BPA) polymer with a similar glass transition temperature (9 °C) as the nematic LCE (4 °C) was also characterized at the same conditions for comparing to the LCE polymers. Based on the loading-unloading stress-strain curves, the energy absorption and dissipation for each material at different strain rates (0.001, 0.1, 1, 10 and 90 s^{-1}) were calculated with considerations of maximum stress and material mass/density. The strain-rate effect on the mechanical response and energy absorption and dissipation behaviors was determined. The energy dissipation ratio was also calculated from the resultant loading and unloading stress-strain curves. All five materials showed significant but different strain rate effects on energy dissipation ratio. The solid LCE and BPA materials showed greater energy dissipation capabilities at both low (0.001 s^{-1}) and high (above 1 s^{-1}) strain rates, but not at the strain rates in between. The polydomain LCE lattice structure showed superior energy dissipation performance compared with the solid polymers especially at high strain rates.

1. Introduction

Liquid crystal elastomers (LCEs) are network polymers with additional functional groups connected to the polymer chains (liquid crystal mesogens) that independently organize into liquid crystal phase, and that phase provides unusual mechanical dissipation capability and actuation behavior for the polymer (Warner et al., 2007). First conceptualized by de Gennes (De Gennes, 1975), LCEs were proposed for artificial muscles and large deformation "soft" (low force) actuators. More recently the literature has seen conceptualization of LCEs for cell scaffolds, interbody fusion cages, soft-active robotics or actuators, and wearable devices (Giamberini et al., 2006; Jiang et al., 2013; Sharma et al., 2017; Prévôt et al., 2018; Ula et al., 2018; Volpe et al., 2020; Hussain et al., 2021; Annapooranan et al., 2022; Liao and Yang, 2022). These applications involve complex mechanical behavior of LCEs which are still being discovered and characterized.

From mechanical perspective, LCEs are typically operated above their glass transition temperature (Luo et al., 2021), and under uniaxial tension or compression, their stress-strain curves exhibit a stress plateau due to re-orientation of the liquid crystal phase via an average

---

re-orientation of the mesogens during deformation (Warner et al., 2007; Luo et al., 2022a). This paper focuses on the behavior of two types of nematic LCEs, namely polydomain and monodomain, and the transition from one to the other under large deformation. In polydomain LCEs, the average mesogen is aligned along the nematic director within a spatial cluster that has a characteristic size much smaller than the size of test articles or engineering components. Different spatial clusters have different nematic director orientations such that, if the nematic director is volume averaged over the characteristic dimensions still small compared to the engineering length scale, there is no preferred nematic director orientation. Polydomain LCEs are mechanical isotropic at least under small to moderate deformations. The second type of LCE focused on in this paper is the nematic monodomain LCE in which there is a single average nematic director aligned over the entire specimen.

Under large deformation, a polydomain LCE transitions to a monodomain state, a.k.a. P-M transition, which has been extensively investigated in the past two decades (Warner et al., 2007; Brand et al., 2006; Patil et al., 2009; Skačej and Zannoni, 2014; Donovan et al.; Yasuoka et al., 2021). The presence of the stress plateau, which is associated with mesogen re-orientation and is often called soft-elasticity, makes the stress-strain response of the LCEs resemble the compressive stress-strain response of foams although the mechanisms are different; shear deformation drives mesogen re-orientation while cell collapse changes porosity in foams (Gibson and Ashby, 1997). Despite the mechanistic differences between solid nematic LCEs and foams, the presence of a stress plateau motivates us to consider LCEs for shock/impact mitigation.

Nematic LCEs have been recently investigated for unusual energy absorption capacity at the macroscale (Mistry et al., 2021a; Jeon et al., 2022; Zhang and Huo, 2022) where it was observed that the LCE response was a strong function of applied strain rate and initial mesogen orientation. At the macroscale, we are considering characteristic lengths on the order of millimeters where fluctuations due to local mesogen microstructure (typically order microns (Ikeda et al., 2003)) have been spatially averaged out, and an average nematic director and scalar order parameter are sufficient to describe the material. We refer to this averaged behavior as macroscale behavior.

Polydomain LCE macroscale behavior is typically isotropic; whereas monodomain LCEs exhibit a significantly anisotropic response. Numerical simulation results of mechanical tensile tests show that, when the tensile loading direction is along the liquid crystal alignment (the direction of nematic director), the monodomain LCEs behave like a regular hyperelastic rubber. However, when the tensile loading direction is off the liquid crystal alignment, an apparent stress plateau and a large loading-unloading hysteresis appear, consequently resulting in a higher efficiency of energy absorption and dissipation (Zhang and Huo, 2022). Based on the same mechanism, one can imagine that, under compression load, the monodomain LCEs may possess higher energy absorption and dissipation when the loading direction is along the direction of nematic director due to the soft elasticity mechanism. For all loading directions, conventional viscoelastic behavior is typically observed. Therefore, soft elasticity and viscoelasticity are simultaneously present in LCE mechanical behavior. Furthermore, foams or lattice structures made from the LCEs add another cellular effect on top of soft elasticity and viscoelasticity for even better energy dissipation and shock mitigation performance (Luo et al., 2021; Traugutt et al., 2020; Mistry et al., 2021b).

Key to understanding LCE energy dissipation is characterizing the mechanical stress-strain response under both loading and unloading. For any material, the dissipated energy per volume can be calculated as the hysteresis under loading-unloading cycle. For viscoelastic materials such as LCEs, this hysteric response is highly strain-rate dependent (Luo et al., 2021). Considering the proposed shock and vibration mitigation applications, understanding the origins of strain rate is needed. However, the study of strain-rate effect on the stress-strain response and energy dissipation of the LCEs and LCE-based lattice structures is limited (Jeon et al., 2022; Zhang and Huo, 2022; Traugutt et al., 2020; Mistry

et al., 2021b; Azoug et al., 2016; Martin Linares et al., 2020). Within the limited studies, the strain-rate effect was mostly investigated within the quasi-static regime (Azoug et al., 2016; Martin Linares et al., 2020). While Mistry et al. (2021b) initiated dynamic characterization with a Kolsky compression bar, that test configuration is not typically suited for measuring the unloading response needed for characterizing the dissipation. Dynamic loading-unloading characterization with a Kolsky compression bar has been attempted for Ni–Ti shape memory alloy and PMMA (Song and Chen, 2004), however, it is not applicable to soft polymers such as the LCEs and their lattice structures investigated in this study. Recently, Ali and Fan developed strain-rate-dependent models for polymers and polymer composites (Ali and Fan, 2020, 2024). After validated with the experimental data at high strain rates, the model was used to predict the unloading behavior of the polymer such that the energy absorption and dissipation were able to be analyzed (Ali and Fan, 2020).

There still exists a gap between the low and high strain rates, a.k.a. intermediate strain rates, for material response characterization. High-speed material testing frames have been recently developed for characterizing material response into intermediate strain rate regime (Othman et al., 2009; Xiao, 2008; Béguelin et al., 1991). However, the nature of "open-loop" operation for such test frames makes it impossible to obtain unloading stress-strain response either. Therefore, current results on energy absorption and dissipation of the LCEs are based on quasi-static loading-unloading stress-strain response which may not be appropriate for shock mitigation or damping analysis in actual environments such as accidental drop, low-to-high velocity crash, or even more severe environments like explosion.

A bench-top high-speed linear actuator has recently been developed at Sandia National Laboratories for characterizing mechanical response of soft materials at the strain rates covering low to intermediate range (Song et al., 2023). This new test capability is operated in a "closed-loop" mode which allows characterization of loading-unloading stress-strain response of soft materials even at the strain rate of hundreds per second. It therefore provides a great opportunity to determine the strain-rate effect on loading-unloading compressive response of the LCEs and their lattice structures, which can be further used to investigate strain rate effect on energy absorption and dissipation.

From the material perspective, the LCEs can be made in a traditional way, such as a multi-staged cast-cure process in order to produce poly or monodomain configurations (Luo et al., 2021, 2022a). Recent additive manufacturing (AM) technology has significantly prompted the fabrication of the LCEs and their lattice structures (Mistry et al., 2021a; Wang et al., 2022a, 2022b, 2023; Peng et al., 2022; Siddiqui et al., 2022). The AM technology for the LCEs usually refers to 3D (Mistry et al., 2021a; Wang et al., 2022b, 2023), such as digital light processing (DLP), direct ink writing (DIW), or even 4D printing with an addition of environmental stimuli such as heat, light, humidity, and electric fields (Wang et al., 2022a; Peng et al., 2022; Siddiqui et al., 2022).

In this study, the recently developed high-speed bench-top linear actuator (Song et al., 2023) was employed to characterize the loading-unloading compressive response of polydomain and monodomain LCE polymers and polydomain LCE lattice structures with two different porosities (nominally, 62% and 85%) at low and intermediate strain rates. A bisphenol-A Di methacrylate (BPADMA, referred to as "BPA" in this study) polymer with a similar glass transition temperature as the nematic LCE was also characterized at the same conditions, as a reference material, for comparing to the LCE polymers. Based on the loading-unloading stress-strain curves, the energy absorption and dissipation for each material at different strain rates (0.001, 0.1, 1, 10 and ~90 s^{-1}) were calculated. The strain-rate effect on the mechanical behavior and energy dissipation was determined and compared to each other.

2. Materials and specimens

The polydomain, monodomain LCEs, and BPA solid polymers were synthesized by casting resin into a glass cylinder. The polydomain and monodomain LCEs were synthesized from the same resin following a modified procedure from Ref. (Saed et al., 2016).

For the polydomain LCE, 39.70 g (68.0 mmol) of diacrylate mesogens RM257 were dissolved in 9.90 g of toluene at 90 °C for 30 min. The solution was then cooled to room temperature and 12.0 g (66.0 mmol) of di-thiol spacer EDDET, 0.47 g (1.1 mmol) of photo-initiator PPO, 0.17 g (0.8 mmol) of inhibitor BHT, and 0.16 g (2.0 mmol) of catalyst TEA were mixed in and degassed. The polydomain resin was then poured into glass cylinders with a diameter of 8.15 mm and left at room temperature overnight to yield a fully polymerized sample. The sample was transferred into a vacuum oven and heated at 80 °C for 12 h to evaporate any residual toluene. These samples were then frozen and cut to about 10 mm in height with a final diameter of 7.8 mm.

The monodomain LCE followed the exact same procedure and chemistry amounts except for 11.40 g of EDDET and an added amount of 0.80 g (2.0 mmol) crosslinker pentaerythritol tektrakis(3-mercaptopriopionate). Once the resin was thoroughly mixed and degassed, it was poured into a glass cylinder with a diameter of 12.5 mm. This glass cylinder was left at room temperature overnight, which resulted in a similar polydomain sample. The sample was transferred into a vacuum oven and heated at 80 °C for 12 h to evaporate any residual toluene. However, once the first stage cure was complete, the sample was extracted from the glass cylinder and stretched and held to 100 % strain with exposure to a 405 nm UV flood light. The sample ended up with a final diameter of 7.7 mm. The mechanical deformation ensured ordering of the mesogens, which produced the monodomain samples. These were cooled down to -18 °C and cut to 10 mm in height for the final sample specifications.

A 0.3 mm slice of the solid monodomain cylinder was also cut to measure the order parameter of the monodomain sample. Using a procedure outlined by Luo et al. (2022b), where the order parameter, $S = (D - 1) / (D + 2)$, is a function of dichroic ratio, $D = A_{max} / A_{min}$, the order parameter was found to be 0.67. This measurement utilized polarized Fourier Transform Infrared Light Spectroscopy (FTIR) with incident polarization angles perpendicular and parallel to the draw orientation. In Fig. 1, the absorptions peaks at the respective polarization angles are reported. A detailed procedure in finding the order parameter utilizing polarized FTIR can be found in Ref. (Luo et al., 2022b).

The BPA polymer was synthesized with the same method as the polydomain samples but replaced the RM257 with 50.00 g (137.20 mmol) of bisphenol-A dimetharcylate. The BPA was then dissolved with 12.50 g of toluene at 90 °C for 30 min. After the solution was cooled to room temperature, 24.80 g (136.01 mmol) of EDDET, 2.59 g (6.19 mmol) of photo-initiator PPO, 0.36 g (0.16 mmol) of inhibitor BHT, and 0.53 g (5.27 mmol) of catalyst TEA were mixed in. Once all chemicals were vigorously mixed in and degassed, the resin was poured into a glass cylinder with a diameter of 8.15 mm and left overnight at room temperature. After the BPA was fully cured, the samples were cooled down to -18 °C then cut to 10 mm in height with a diameter of 7.8 mm for individual test specimens (see Fig. 2).

The polydomain Z-12 lattice structures were synthesized using a commercial masked stereolithography (MSLA) 3D printer, Anycubic Photon Mono X. In preparation of the resin, 96.60 g (164.1 mmol) of diacrylate mesogens 1,4-Bis- [4-(3- acryloyloxypropyloxy) benzoyloxy] -2-methylbenzene (RM257) were dissolved in 152.50 g of toluene at 90 °C for 30 min. After cooled to room temperature, 30.00 g (164.1 mmol) of di-thiol spacer 2,2′-(ethylenedioxy) diethanethiol (EDDET), 6.10 g (1.5 mmol) of photo-initiator phenlybis(2,4,6-trimethylbenzoly) phosphine oxide (PPO), 0.73 g (3.3 mmol) of inhibitor butylated hydroxytoluene (BHT), and 1.20 g (11.9 mmol) of catalyst triethylamine (TEA) were mixed in the solution. To ensure timely oligomer formation, this solution was degassed and heated to 100 °C for 2 h. After cooled to room temperature, the solution was poured into a vat for the 3D printer and ready for print. The print parameters followed as such: 50 μm layer height, 200 μm initial layer height, 7.6 s layer-to-layer cure time, and 30 s initial layer cure time. Once the lattices were printed, they were rinsed with isopropyl alcohol and sonicated for 30 s. This ensured no residual resin trapped within the lattice structure. After cleaning, they were exposed to a 405 nm UV flood light to fully polymerize the samples. The sample was transferred into a vacuum oven and heated at 80 °C for 12 h to evaporate any residual toluene. The lattice structure was designed in SolidWorks® with two nominal porosities: 62% and 85%. After printing the actual porosities of the lattice structures were measured to be 50.8% and 73.7%, respectively, which were ~11% lower than the nominal values. In this study, we used the nominal values (62% and 85%) to distinguish the two lattice structures. The lattice structures for both porosities had a cubic shape with dimensions of 13 × 13 × 13 mm as seen in Fig. 2.

3. Experiments

The compressive experiments on all five materials were conducted with a bench-top high-speed linear actuator that is presented in Ref. (Song et al., 2023). As shown in Fig. 3, the test system consists of a Rexroth® high-speed electromechanical actuator to which a front platen was connected via an adapting rod. Another identical platen was installed on a Kistler load cell mounted on a back plate. The Kistler load cell was used to measure the force history on the specimen during mechanical loading. A customized laser extensometer (Nie et al., 2015) was installed to directly measure the displacement of the actuator such that the specimen strain can be calculated. The compressive stress-strain curve of the material under investigation was then obtained. The linear actuator has a maximum velocity of ~1.9 m/s with a closed-loop operation mode, enabling loading-unloading stress-strain characterization at the strain rates up to 100 s^{-1} for the specimen design in this study. The signals from the load cell and the laser extensometer were acquired with a LeCroy digital oscilloscope.

Fig. 4 shows a typical oscilloscope record of force and displacement histories in a polydomain LCE polymer at a strain rate of 10 s^{-1}. Prior to mechanical loading, the polydomain LCE specimen was attached to the back platen with a thin layer of thermal joint compound. The grease was used to hold the specimen on the platen before being loaded and to lubricate the interface during compression. Before testing, the actuator
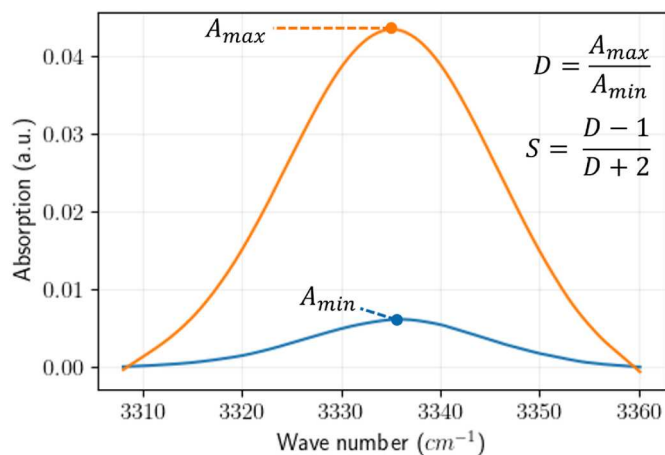

Fig. 1. Plot of the polarized FTIR absorption peaks for the C–H stretching modes for polarization angles perpendicular (orange) and parallel (blue) to the mesogen orientation. The listed equations can be used to find the order parameter following Luo et al. (Luo et al., 2022b). (For interpretation of the references to colour in this figure legend, the reader is referred to the Web version of this article.)
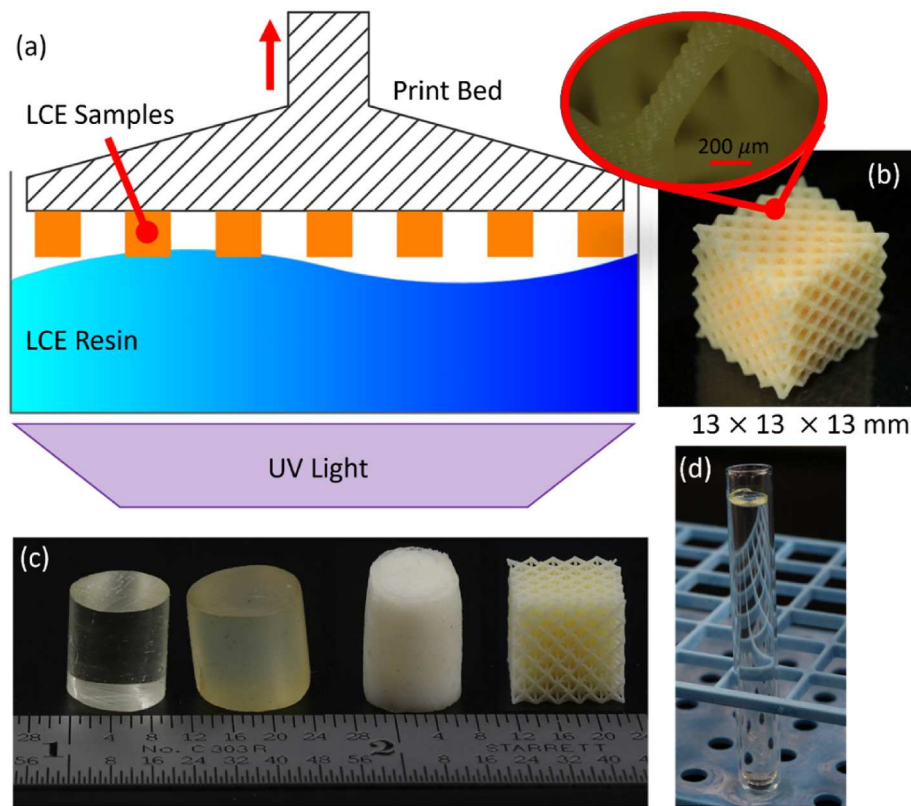
Fig. 2. Illustration of 3D Printing process and actual photos of specimens. (a) 3D printing process of the polydomain LCE lattice structures. (b) Actual photo of the polydomain LCE lattice specimen. (c) BPA, monodomain, polydomain cylinders, and the polydomain lattice from left to right. (d) Example BPA cylinder in its curing procedure.
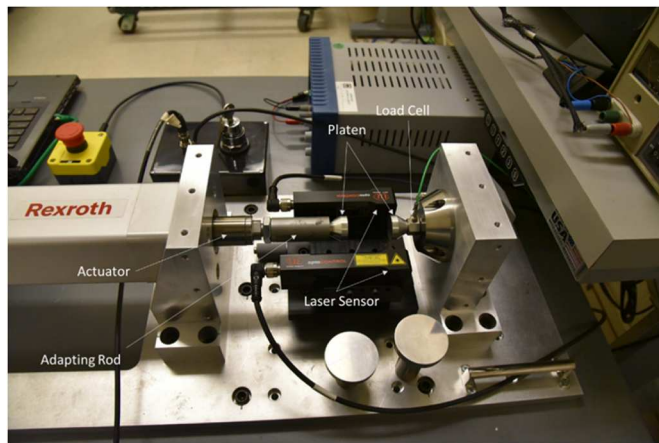

Fig. 3. Photograph of the bench-top high-speed linear actuator (Song et al., 2023).

Fig. 4. Typical oscilloscope records of load cell and laser extensometer during a compression test of a polydomain LCE specimen at $10\ \text{s}^{-1}$.

was intentionally left at a distance from the specimen to accelerate the platen to the desired velocity before making specimen contact. The laser extensometer signal shown in Fig. 4 indicates that the actuator took ~0.2 s before it touched the specimen. The specimen was then compressed for 0.06 s with increasing load cell output until the unloading stage of the test was started. The actuator had a maximum acceleration of ~400 g. This makes the "turn-around" time as short as 50 μs from loading to unloading at the strain rate of $10\ \text{s}^{-1}$, which is negligible as shown in Fig. 4. Even at the strain rate of $90\ \text{s}^{-1}$, it takes approximately 0.5 ms from loading to unloading, which is ~5% of the loading duration. The unloading portion followed the same strain rate as the loading portion, but the load cell signal dropped to zero prior to the specimen
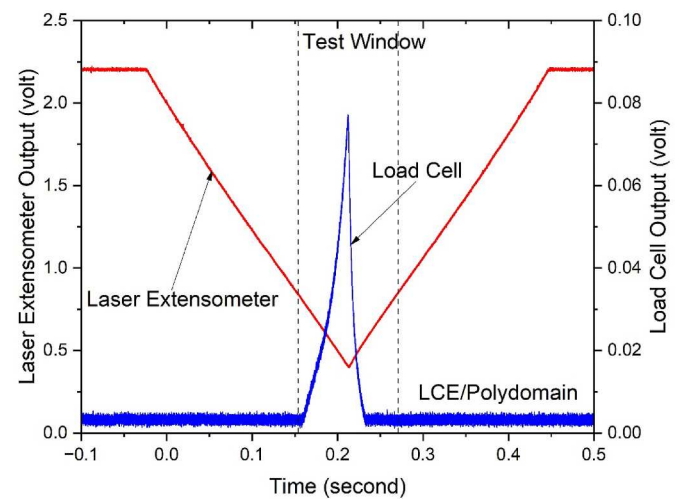
returning to zero strain, a typical signature of viscoelasticity.

Fig. 5 shows the loading and unloading stress-strain curves of a polydomain LCE polymer at the strain rate of $10\ \text{s}^{-1}$, which was calculated from Fig. 4. The polydomain LCE polymer exhibits a typical viscoelastic response with significant hysteretic stress-strain behavior. The loading stress-strain response shows a nearly linear response until 25% strain and then strain stiffens. The unloading stress-strain response has a higher slope than the loading response at equivalent axial strains and reaches zero load at 33% nominal compressive strain at this strain rate.
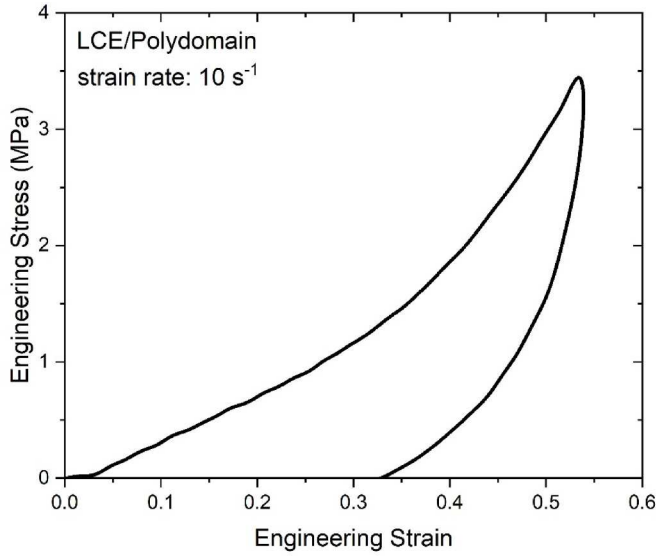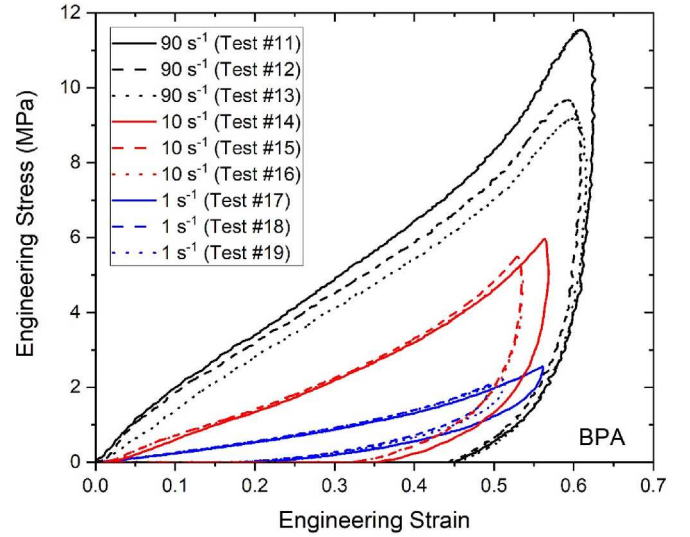
Fig. 5. Compressive stress-strain curve of a polydomain LCE specimen during loading and unloading at the same strain rate of 10 s^{-1}.

4. Experimental results

Following the same procedure, the BPA polymer (as a reference material), polydomain and monodomain LCE polymers, and polydomain LCE lattice structures with two porosities (nominally, 62% and 85%) were characterized at five strain rates of 0.001, 0.1, 1, 10, and ~90 s^{-1}. A new specimen was used for each individual test. The BPA, polydomain and monodomain LCE solid polymers were compressed to ~50% strain; whereas the polydomain LCE lattice structures were compressed to ~80% strain. It is noted that the actual maximum strains slightly varied due to specimen variation in dimensions and linear actuator control especially at higher strain rates. We note that the loading direction was aligned with the nematic director for the solid monodomain LCE polymers. Two to three tests were repeated for each strain rate and material combination, and good repeatability was observed. The loading and unloading stress-strain curves of the five materials are shown in Figs. 6–10, respectively. Due to significant strain-rate effect, the resultant stress-strain curves were plotted in two figures using the results at 1 s^{-1} as a division to ensure sufficient resolution within the entire strain-rate range. No visible crack or failure was observed in the specimens after mechanical testing. It took the specimens minutes to hours to recover back to their original shapes, depending on the material and maximum strains subjected to the specimens.

The solid BPA (Fig. 6) and polydomain LCE (Fig. 7) polymers show similar viscoelastic stress-strain responses and hysteresis behaviors. At certain strains, the stress levels were comparable between the two materials. The BPA had larger hysteresis than the polydomain LCE although the glass transitions were not identical, so it is difficult to compare them quantitatively. Instead, qualitatively, these results suggest that for these polydomain LCEs, the role of nematic director alignment during deformation cannot be distinguished from conventional viscoelastic behavior if one studies the load-unload mechanical response alone.

In comparison to the solid BPA and polydomain LCE, the solid monodomain LCE exhibited a stress plateau during compression at all strain rates in Fig. 8. This may indicate that the rotation/re-alignment of the mesogens in the monodomain LCE during compression is significant compared with normal viscoelastic polymer chain mechanics. While the three stages of loading are clear at low rates in Fig. 8(a–b), which include an initially stiff elastic behavior, a plateau, and a strain stiffening region, the tests show more variation at the strain rate of 90 s^{-1} in Fig. 8(a) in which these three regimes are not present for all specimens. The origins of this variation are not yet determined but may be related to

(a)
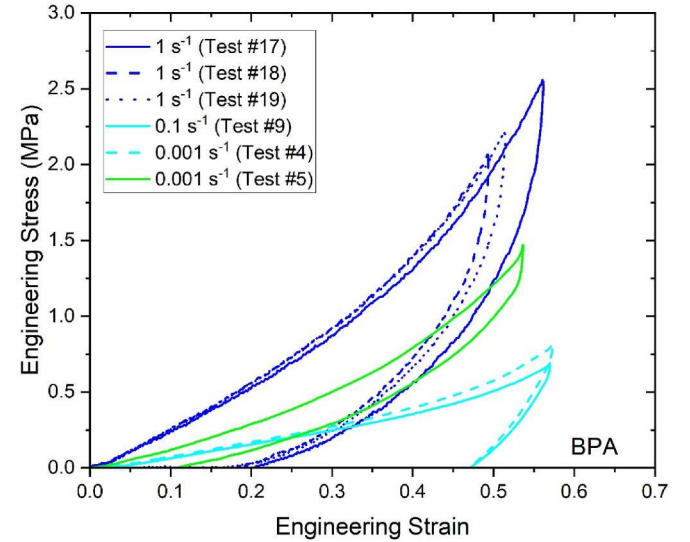
(b)

Fig. 6. Compressive stress-strain curves of the BPA polymer at various strain rates.

specimen preparation. This mesogen re-alignment (soft elasticity) process reduced the material stress/stiffness of the material at a given strain when compared with the solid polydomain or BPA specimens in Figs. 7 and 6 nearly by a factor of -2.

The LCE lattices in Figs. 9 and 10 exhibit typical stress-strain responses of foam materials: a linear elastic response followed by a long stress plateau and then a sudden stiffening with densification. It is noted that these three regimes of behavior in the polydomain LCE lattice structures are the same as in typical cellular structures, as observed and shown in Fig. 11. The role of mesogen rotation in the polydomain LCE lattice structures throughout the stress-strain curve appears to be negligible or at least cannot be determined from these data in Figs. 9 and 10 alone. Due to higher porosity, the plateau stresses in the 85%-porosity LCE lattice structure were much lower than those in the 62%-porosity LCE lattice structure as expected from standard Gibson and Ashby scaling considerations (Gibson and Ashby, 1997).

It is not surprised to observe the significant strain-rate effect for the materials due to their viscoelastic nature. The monodomain LCE had
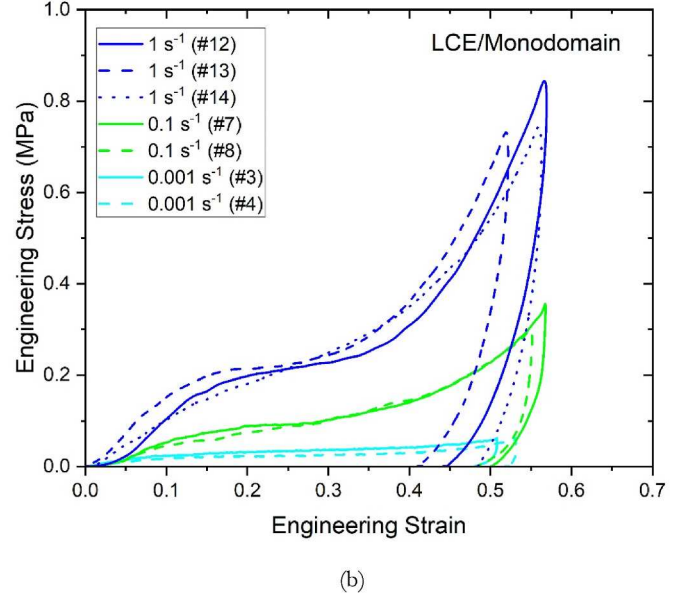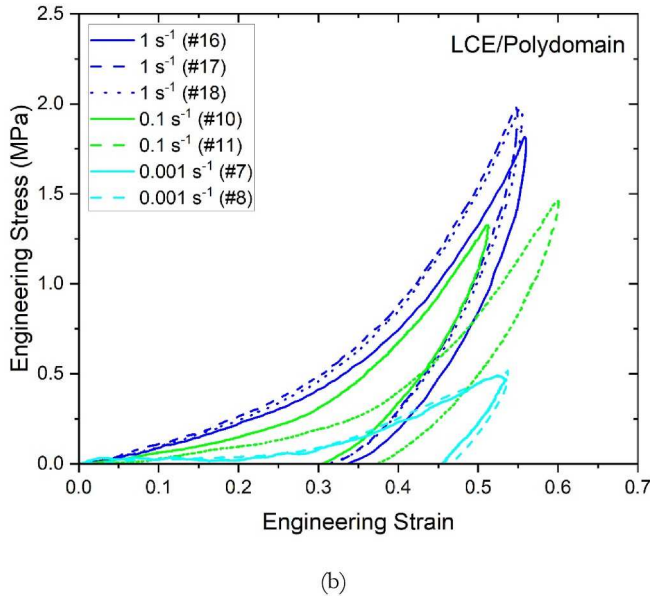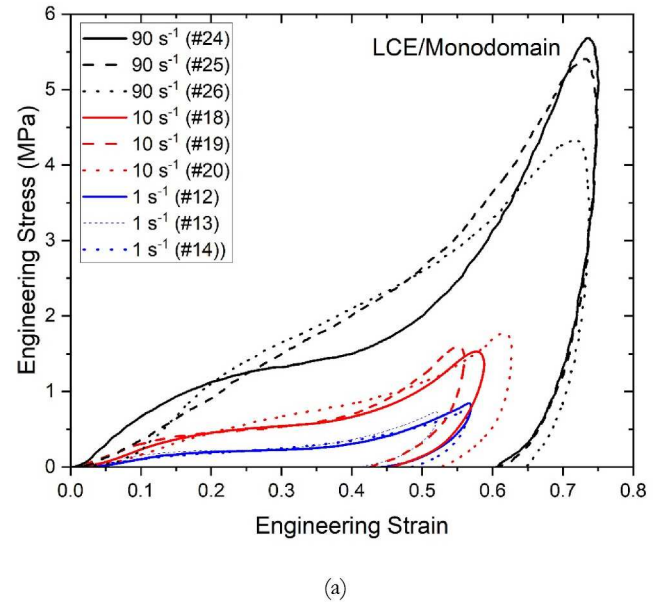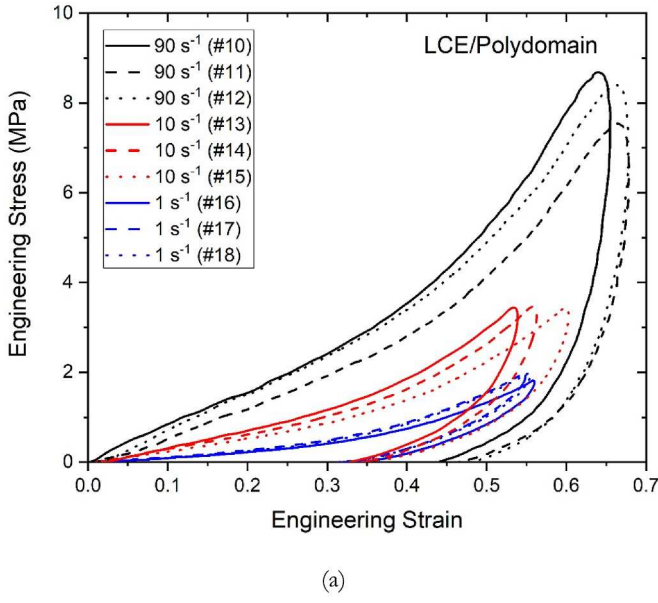
(a)

(b)

Fig. 7. Compressive stress-strain curves of the polydomain LCE polymer at various strain rates.

(a)

(b)

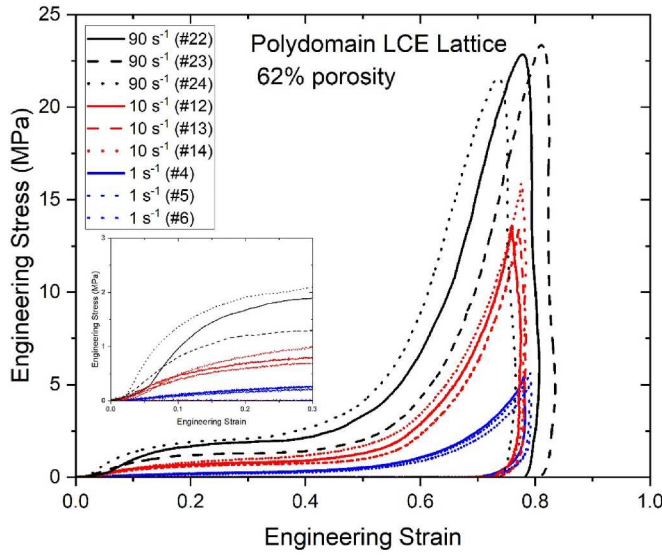**Fig. 8.** Compressive stress-strain curves of the monodomain LCE polymer at various strain rates.

more significant strain-rate dependency than the BPA and polydomain LCE because of the interplay of two mechanisms - viscoelasticity versus mesogen rotation – in the monodomain LCE (Chung et al., 2024). When the solid polymers were made into lattice structures, the strain-rate effect of structural response will be added on top of the strain-rate effect of viscoelastic material response, making the overall strain-rate effect more pronounced. In order to quantify and compare the strain-rate effects in all five materials, we defined a specific strain rate normalization in which the stress at the nominal compressive strain of 0.40 during loading was normalized to the stress at the same strain but at the strain rate of 0.001 s^{-1} (during loading). This normalized stress is like the definition of dynamic increase factor (DIF) for brittle materials such as concrete. Fig. 12 shows a log-log plot of the normalized stresses versus strain rate for all five materials. A linear relationship was observed, and the slope represents the strain-rate sensitivity, γ,

$$\gamma = \frac{d \log \frac{\sigma}{\sigma_0}}{d \log \frac{\dot{\varepsilon}}{\dot{\varepsilon}_0}} = \frac{d \log \sigma}{d \log \dot{\varepsilon}} \tag{1}$$

where σ_0 is the stress at 40% nominal compressive strain at the reference strain rate $\dot{\varepsilon}_0 = 0.001$ s^{-1}. Table 1 lists the value of γ for the five materials. As shown in Fig. 12 and Table 1, the polydomain LCE had a close strain-rate sensitivity to the BPA as expected from qualitative analyses of Figs. 6 and 7. The polydomain LCE lattice structures had the highest strain-rate sensitivities which are insignificantly dependent on the material porosity at least for the two porosities studied here. The strain-rate sensitivity of the monodomain LCE was lower than the polydomain LCE lattice structures but higher than the polydomain LCE and BPA. All strain-rate sensitivities appear to be well approximated by a linear relationship on a log-log plot suggesting a power law relationship for the strain rate is reasonable for the materials here and validating the usage of Equation (1).

4.1. Energy absorption and dissipation

Based on the loading and unloading stress-strain curves shown in Figs. 5–9, the absorbed energy, E_{abs}, per unit volume, was calculated
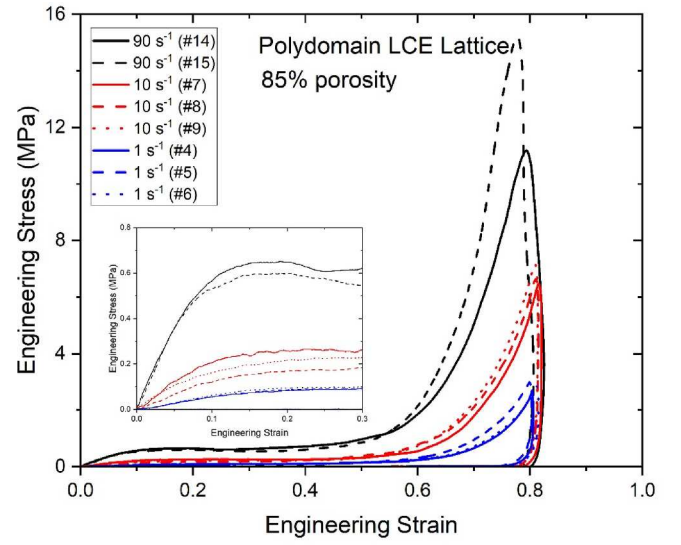
(a)
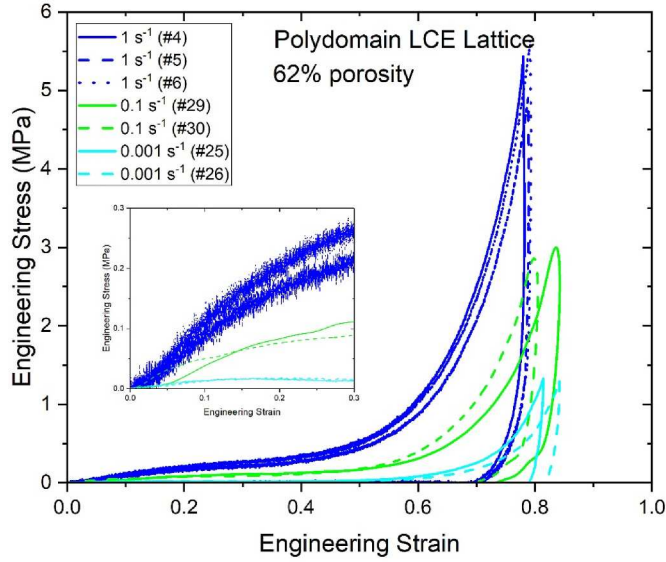
(b)

Fig. 9. Compressive stress-strain curves of the 62%-porosity polydomain LCE lattice at various strain rates.
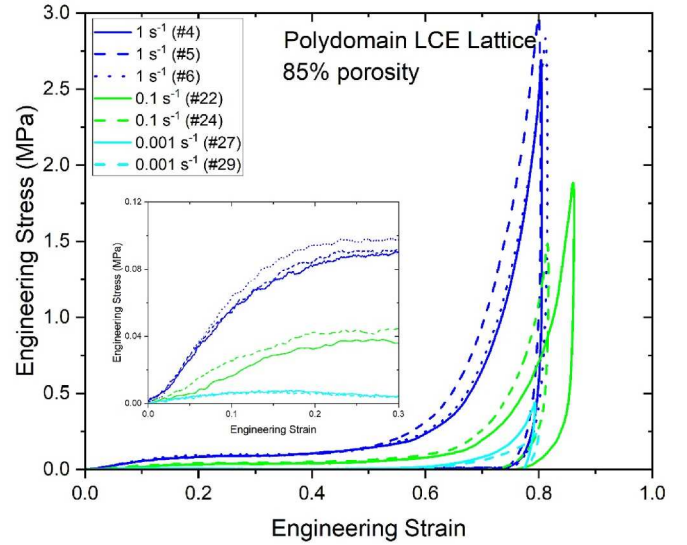
with

$$E_{abs} = \int_{loading} \sigma(\varepsilon)d\varepsilon \qquad (2)$$

The absorbed energy per unit volume is the integrated area under the loading stress-strain curve.

Equation (2) describes the energy absorption capacity that is commonly used for foam materials (Gibson and Ashby, 1997). Fig. 13 shows the energy absorption at various strain rates for the five materials under investigation. In general, a better energy absorption performance means a greater energy absorption at a certain stress, or a lower stress for a certain energy absorption. Therefore, the BPA shows better energy absorption performance with decreasing strain rate, when the stress level is lower than 6 MPa because the slope of the energy absorption capability against strain is higher. When the stress level is higher than 6 MPa, the absorbed energy curves approximately approach the same line (dotted line) – the absorbed energy linearly increased with increasing

(a)

(b)

Fig. 10. Compressive stress-strain curves of the 85%-porosity polydomain LCE lattice at various strain rates.

stress regardless of strain rate. The polydomain LCE showed quite similar behavior to the BPA, but with less of a strain-rate effect. The dotted lines in Fig. 13(a) and (b) represent the nearly linear energy absorption capacity with stress.

The monodomain LCE and polydomain lattice structures showed quite similar "S" shapes on the energy absorption curves although the mechanisms are different. Such an "S" shape is typical for foam materials (Gibson and Ashby, 1997). But the similar "S" shape observed in solid monodomain LCE was due to mesogen rotation. According to Gibson and Ashby(Gibson and Ashby, 1997), the upper turning point ("shoulder") on the "S" shape indicates the optimized (most effective) energy absorption capacity. Connecting the upper turning points at different strain rates provides an envelope of energy absorption capacity for the materials, as indicated with the dotted line. The slopes of the dotted lines shown in Fig. 13 may be used to compare the optimized energy absorption capacities for all five materials: a higher slope yields a better energy absorption performance.

In this study, we defined dimensionless energy absorption factor, λ, as the slope of the absorbed energy per unit volume vs. stress curves,
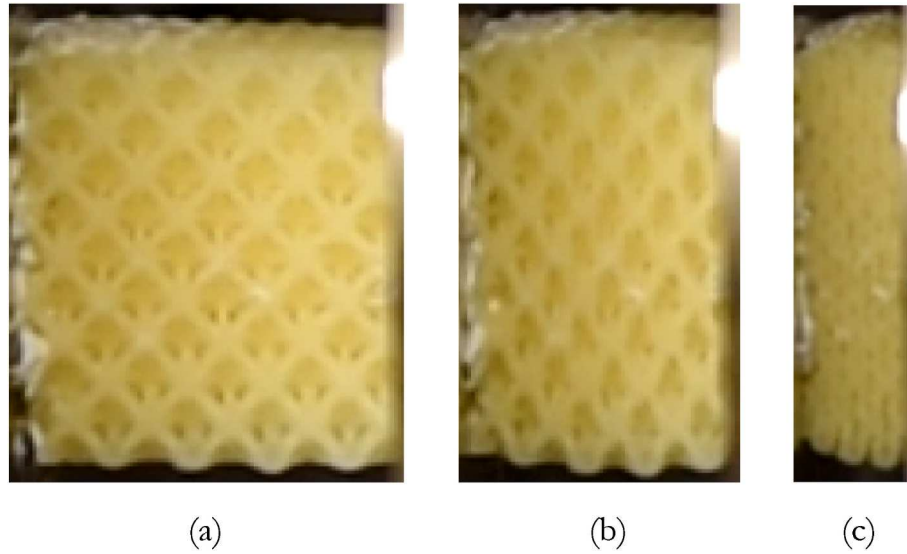
Fig. 11. Photos of a polydomain LCE lattice during compression. (a) original; (b) lattice buckling; (c) densification.
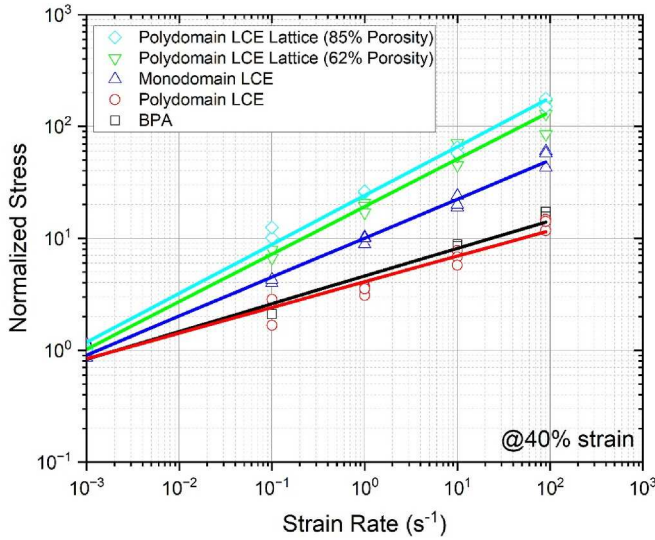

Fig. 12. Strain rate effect on normalized stress at a certain strain of 40%.

which are tabulated in Table 1 for the five materials. Table 1 shows the 85%-porosity polydomain LCE lattice structure had the best energy absorption performance; whereas, the solid polydomain LCE was the worst. The BPA, monodomain LCE, and 62%-porosity polydomain LCE lattice structure had very similar energy absorption performances. Particularly, although the mechanisms are different, the solid mono-domain LCE had a very close energy absorption performance to the 62%-porosity polydomain LCE lattice structure. This means the mesogen effect played a nearly equal role to the cellular effect with 62% porosity in terms of energy absorption.

The material absorbs energy during deformation but part of the absorbed energy will be released during recovery/unloading process. The difference between the absorbed energy and the released energy

represents the energy that is dissipated,

$$E_{diss} = E_{abs} - \int_{unloading} \sigma(\varepsilon)d\varepsilon = \int_{loading} \sigma(\varepsilon)d\varepsilon - \int_{unloading} \sigma(\varepsilon)d\varepsilon \quad (3)$$

where the dissipated energy per unit volume, E_{diss}, is the integrated area between the loading and unloading stress-strain curves. The dissipated energy indicates the intrinsic energy dissipation capacity of materials under constant-strain-rate cyclic loading.

Fig. 14 shows the comparison of absorbed and dissipated energies per unit volume for the five materials at various strain rates. It is noted that both absorbed and dissipated energies were calculated based on the maximum strains which were ~50% for the BPA, polydomain LCE, and monodomain LCE but 80% for the polydomain LCE lattice structures. Therefore, it may not be appropriate to directly compare the solids to the lattice structures, although they all are plotted in Fig. 14. In general, all five materials showed significant strain-rate effect on absorbed and dissipated energies due to strain-rate-dependent stress-strain response discussed earlier. Among the three solid polymers, the BPA had the highest absorbed and dissipated energies, whereas, the monodomain LCE had the lowest absorbed and dissipated energies. Between the two lattice structures, the 85%-porosity lattice structure had lower absorbed and dissipated energies than the 62%-porosity lattice structure. All these seem to be contrary to the energy absorption factors listed in Table 1. This is because the maximum stress was not accounted for in Fig. 14.

Fig. 15 shows the normalized energies by the maximum stress for the five materials. Again, it is not appropriate to directly compare the solid polymers to the lattice structures due to different maximum compression strains. The three polymers showed quite similar normalized energies, especially at the strain rates higher than 0.1 s^{-1}, which is consistent with the energy absorption factors shown in Table 1. The two lattice structures showed a mixed trend of the normalized energy at different strain rates. At the strain rates of 0.001 and 10 s^{-1}, the two lattice structures had very similar normalized energies. In comparison to the 85%-porosity polydomain LCE lattice structure, the 62%-porosity polydomain LCE lattice structure showed higher normalized energies for the strain rates between 0.001 and 10 s^{-1}, but lower normalized energy at

Table 1
Strain rate sensitivity of the five materials.

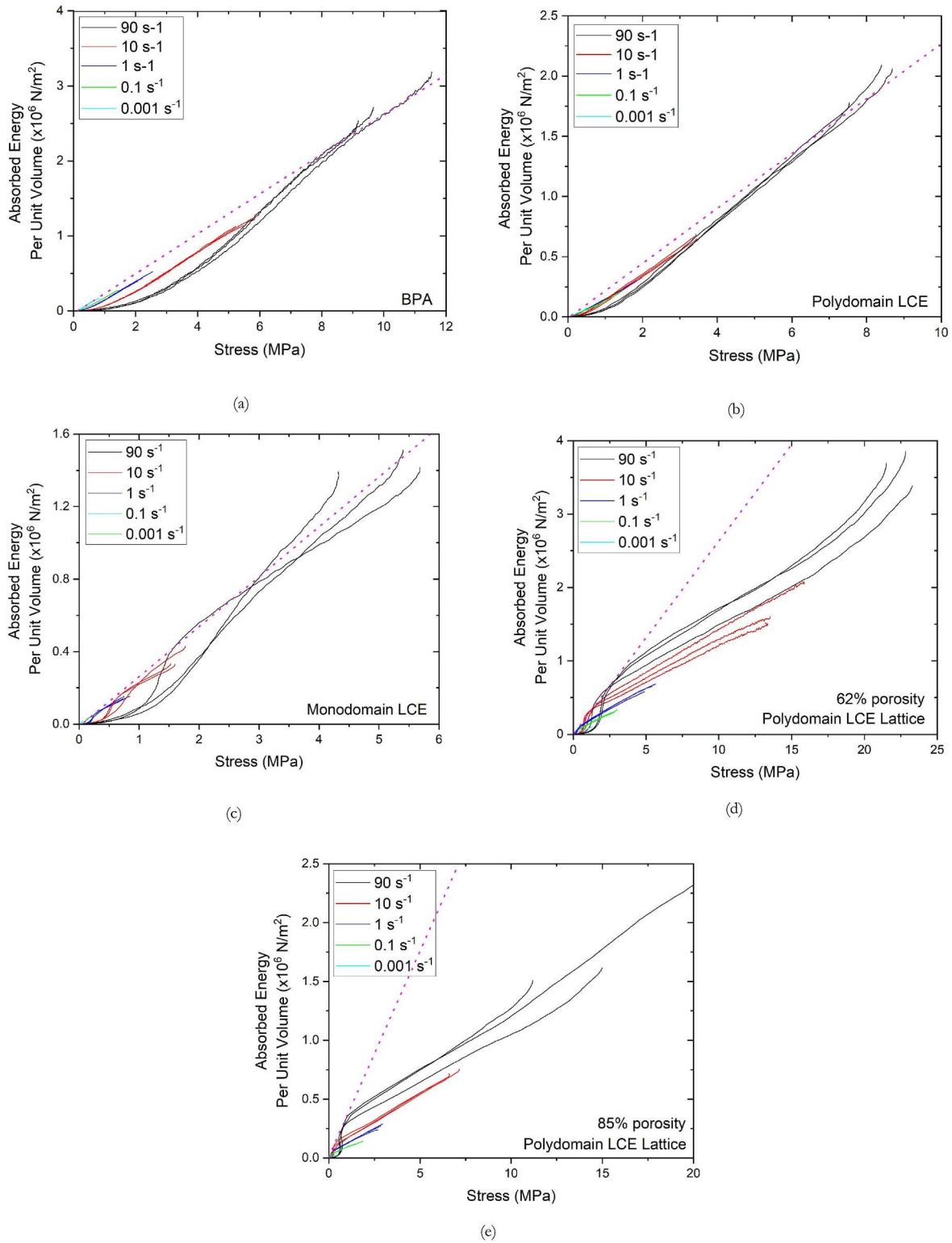| Material	BPA	Polydomain LCE	Monodomain LCE	Polydomain LCE Lattice (62% porosity)	Polydomain LCE Lattice (85% porosity)
Strain Rate Sensitivity, γ (MPa·s)	0.2473	0.2293	0.3479	0.4245	0.4369
Energy Absorption Factor, λ	0.2650	0.2278	0.2726	0.2628	0.3513

Fig. 13. Energy absorption capacity at various strain rates. (a) BPA; (b) polydomain LCE; (c) monodomain LCE; (d) polydomain LCE lattice – 62% porosity; (e) polydomain LCE lattice – 85% porosity. The pink dotted lines indicate the envelopes of energy absorption capacity for the individual materials. (For interpretation of the references to colour in this figure legend, the reader is referred to the Web version of this article)

the highest strain rate of 90 s^{-1}. In general, the energy absorption factors in Table 1 may be the best to provide an overall comparison of the energy absorption capacity for the five materials.

Mass/weight is an important factor in engineering design of components. A good shock/impact mitigation material is desired to absorb or dissipate energy as much as possible but with minimum mass/weight. Normalizing the absorbed/dissipated energies per unit volume by density yields absorbed/dissipated energy per unit mass. A higher normalized energy per unit mass indicates more efficient and effective energy absorption/dissipation. Fig. 16 shows the energy absorption and
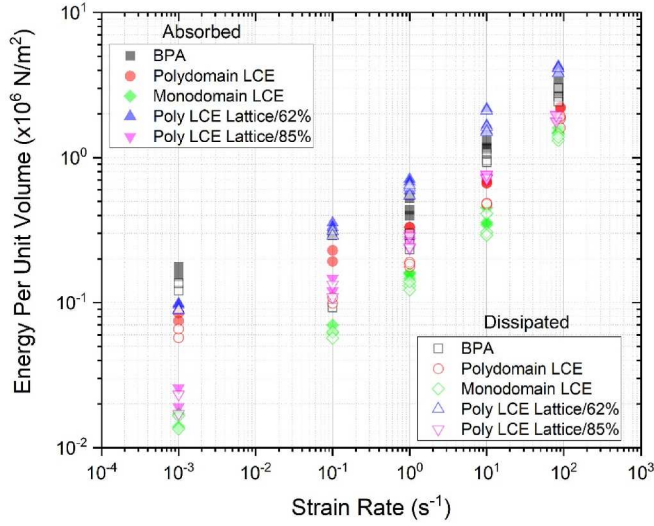
Fig. 14. Comparison of the absorbed and dissipated energies per unit volume at various strain rates for the five materials.

Fig. 15. Comparison of the normalized absorbed and dissipated energies per unit volume by maximum stress at various strain rates for the five materials.
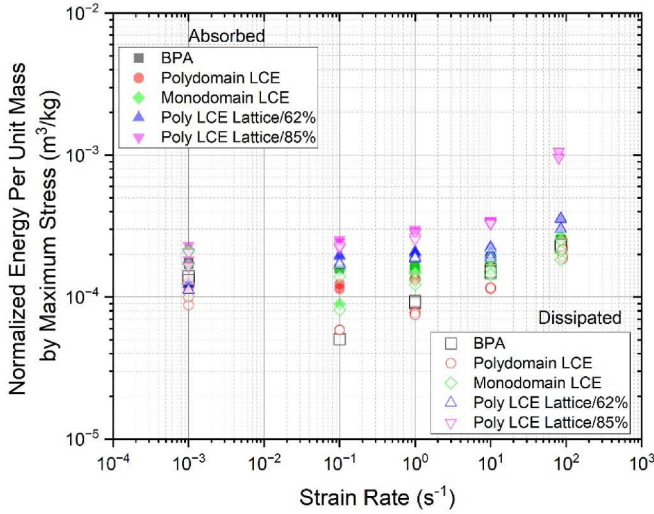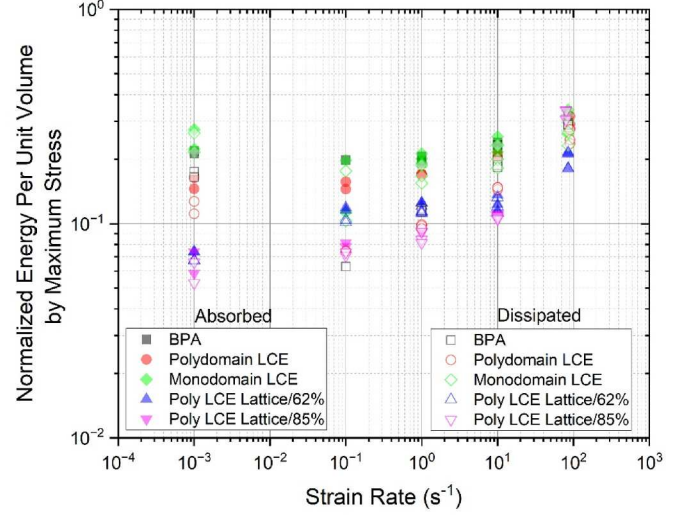

Fig. 16. Comparison of the normalized absorbed and dissipated energies per unit mass by maximum stress at various strain rates for the five materials.

dissipation per unit mass for the five materials at different strain rates. After material mass/weight is under consideration, the 85%-porosity polydomain LCE lattice structure showed the highest energy absorption and dissipation among the five materials, particularly at higher strain rates. The 62%-porosity polydomain LCE lattice structure also showed higher energy absorption and dissipation than the solid polymers when strain rate is 10^{-1} s^{-1} or above. It is noted that at the strain rates between 10^{-1} and 10 s^{-1}, the absorbed energy for the 62%-porosity polydomain LCE lattice was just slightly higher than that for the monodomain LCE. However, at the lowest strain rate of 10^{-3} s^{-1}, the monodomain LCE showed the highest energy absorption and dissipation among all five materials. All these observations mean that, at a higher strain rate, i.e., 90 s^{-1}, the cellular effect dominates the energy absorption and dissipation. At the lowest strain rate, i.e., 10^{-3} s^{-1}, the soft-elasticity (mesogen rotation/re-alignment) dominates the energy absorption and dissipation. When strain rates are between 0.001 and 90 s^{-1}, the 85%-porosity polydomain LCE lattice still shows the highest energy absorption and dissipation. However, the 62%-porosity polydomain LCE lattice exhibits very close energy absorption and dissipation

to the monodomain LCE, indicating an equivalency between the cellular effect (for the 62% porosity) and soft elasticity effect.

The ratio of the dissipated energy to the absorbed energy yields a dimensionless energy dissipation ratio,

$$\delta = \frac{E_{diss}}{E_{abs}} = 1 - \frac{\int_{unloading} \sigma(\varepsilon)d\varepsilon}{\int_{loading} \sigma(\varepsilon)d\varepsilon} \tag{4}$$

This energy dissipation ratio represents the intrinsic energy dissipation capability of the material. Fig. 17 compares the energy dissipation ratios at various strain rates for the five materials. The BPA and polydomain LCE had very similar strain-rate effect on the energy dissipation ratio. At the strain rate of 0.001 s^{-1}, both materials had energy dissipation ratios around 0.8. When the strain rate increased to 0.1 s^{-1}, the energy dissipation ratios decreased to 0.32 and ~0.5 for the BPA and polydomain LCE, respectively. With further increase of strain rate, the energy dissipation ratios for the BPA and polydomain LCE increased. The monodomain LCE showed similar trend but the lowest energy dissipation ratio (~0.85) at the strain rate of 1 s^{-1}. All BPA, polydomain LCE, and monodomain LCE had a very close energy dissipation ratio (~0.90) at the strain rate of 90 s^{-1}, which suggests that viscoelasticity
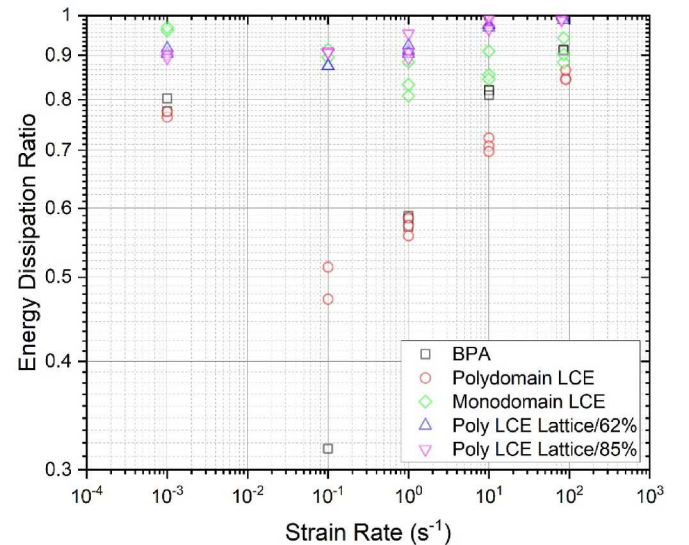

Fig. 17. Energy dissipation ratios of the five materials at various strain rates.

becomes dominant over the nematic director reorientation mechanism at higher strain rates (since all materials had similar Tgs and approximately similar viscoelastic behavior at room temperature). Although the porosities were different, the polydomain LCE lattice structures show very similar characteristic of energy dissipation ratio. When strain rate was below 1 s^{-1} the energy dissipation ratio was the same (~0.90) for both polydomain LCE lattice structures, indicating minimal strain-rate effect. When strain rate is above 1 s^{-1}, the energy dissipation ratio increased with increasing strain rate. At the strain rate of 90 s^{-1}, nearly 100% energy was dissipated in the polydomain LCE lattice structures, which indicates that the polydomain LCE lattice structures had an excellent performance to mitigate external shock and impact. It is noted that, at the strain rate of 0.001 s^{-1}, the monodomain LCE had the highest energy dissipation ratio among the materials including the lattice structures. This suggests that nematic director re-orientation (soft elasticity) dominates the material response at low strain rates, but still warrant further investigation on the strain-rate effect. These observations are consistent with those observed in Fig. 15.

5. Conclusions

3D printed polydomain LCE, monodomain LCE, and two polydomain LCE lattice structures with 62% and 85% porosities were mechanically characterized in compression with a high-speed linear actuator that enabled exploration of the load-unload behavior of these materials from 10^{-3} and 10^2 s^{-1}. A BPA polymer was also characterized as a reference material. All five materials showed significant strain-rate effect. Energy calculation and analysis, including energy absorption and dissipation per unit volume, normalized energy absorption, and dissipation per unit volume by maximum stress, and normalized energy absorption and dissipation per unit mass by maximum stress, were then conducted and compared at various strain rates for the five materials, which may be applicable for different shock mitigation design usages. Energy dissipation ratio was calculated from the resultant loading and unloading stress-strain curves. All five materials showed significant but different strain-rate effects on energy dissipation ratio. In general, the solid LCE and BPA materials showed great energy dissipation capabilities at both low (0.001 s^{-1}) and high (above 1 s^{-1}) strain rates, but not at the strain rates in between. The polydomain LCE lattice structure showed superior energy dissipation performance compared with the solid polymers.

For LCE polymers, viscoelasticity and soft elasticity effect are dominant factors for strain-rate-dependent energy absorption and dissipation. However, the role of soft elasticity due to nematic director re-orientation was only clearly observed in the mechanical behavior of the monodomain LCEs. The solid polydomain LCE mechanical behavior did not show distinct behavior compared with the BPA reference polymer.

When lattice structures were made from the LCE polymers, the cellular effect became an additional factor to contribute strain-rate-dependent energy absorption and dissipation. At low strain rates, the soft elastic response of the monodomain LCE behavior produced the most favorable energy dissipation behaviors (when normalized), but at high rates, the cellular effect dominated over the soft elastic mechanism.

From a practical standpoint, we observe that LCEs did not afford clear advantage at high strain rates compared with elastomeric lattices, but at slow rates, the monodomain LCE when loaded along the director direction provided superior energy absorption and dissipation behavior. Under no circumstances did the solid polydomain LCE outperform any of the other materials studied.

CRediT authorship contribution statement

Bo Song: Writing – original draft, Formal analysis, Conceptualization. **Dylan Landry:** Methodology, Investigation. **Thomas Martinez:** Methodology, Investigation. **Christopher N. Chung:** Methodology, Investigation, Conceptualization. **Kevin N. Long:** Writing – review &

editing, Project administration, Methodology, Funding acquisition, Conceptualization. **Kai Yu:** Writing – review & editing, Supervision, Methodology, Investigation, Funding acquisition. **Christopher M. Yakacki:** Writing – review & editing, Supervision, Resources, Methodology.

Declaration of competing interest

The authors declare that they have no known competing financial interests or personal relationships that could have appeared to influence the work reported in this paper.

Data availability

Data will be made available on request.

References

Ali, S.F., Fan, J., 2020. Elastic-viscoelastic constitutive model for capturing the mechanical response of polymer composite at various strain rates. J. Mater. Sci. Technol. 57, 12–17.

Ali, S.F., Fan, J., 2024. Mechanism-based modeling of strain rate-dependent transition of micromechanical behavior accompanied by temperature rise effects of a toughened polymer composite. J. Mater. Eng. 150, 04024015.

Annapooranan, R., Wang, Y., Cai, S., 2022. Highly durable and tough liquid crystal elastomers. ACS Appl. Mater. Interfaces 14, 2006–2014.

Azoug, A., Vasconcellos, V., Dooling, J., Saed, M., Yakacki, C.M., Nguyen, T.D., 2016. Viscoelasticity of the polydomain-monodomain transition in main-chain liquid crystal elastomers. Polymer 98, 165–171.

Béguelin, P., Barbezat, M., Kausch, H.H., 1991. Mechanical characterization of polymers and composites with a servohydraulic high-speed tensile tester. Journal de Physique III France 1, 1867–1880.

Brand, H.R., Pleiner, H., Martinoty, P., 2006. Selected macroscopic properties of liquid crystalline elastomers. Soft Matter 2, 182–189.

Chung, C., Luo, C., Yakacki, C.M., Song, B., Long, K., Yu, K., 2024. Revealing the unusual rate-dependent mechanical behaviors of nematic liquid crystal elastomers. Int. J. Solid Struct. 292, 112712.

De Gennes, P.-G., 1975. Réflexions sur un type de polymers nématiques. Comptes Rendus de l'Académie des Sciences B281, 101–103.

Donovan, B.R., Fowler, H.E., Matavulj, V.M., and White, T.J., Mechanotropic elastomers, Angew. Chem. Int. Ed., 58:13744-13748.

Giamberini, M., Ambrogi, V., Cerruti, P., Carfagna, C., 2006. Viscoelasticity of main chain liquid crystalline elastomers. Polymer 47, 4490–4496.

Gibson, L.J., Ashby, M.F., 1997. Cellular Solids: Structures and Properties. Cambridge University Press.

Hussain, M., Jull, E.I.L., Mandle, R.J., Raistrick, T., Hine, P.J., Gleeson, H.F., 2021. Liquid crystal elastomers for biological applications. Nanomaterials 11, 813.

Ikeda, T., Nakano, M., Yu, Y., Tsutsumi, O., Kanazawa, A., 2003. Anisotropic bending and unbending behavior of azobenzene liquid-crystalline gels by light exposure. Adv. Mater. 15, 201–205.

Jeon, S.-Y., Shen, B., Traugutt, N.A., Zhu, Z., Fang, L., Yakacki, C.M., Nguyen, T.D., Kang, S.H., 2022. Synergistic energy absorption mechanisms of architected liquid crystal elastomers. Adv. Mater. 34, 2200272.

Jiang, H., Li, C., Huang, X., 2013. Actuators based on liquid crystalline elastomer materials. Nanoscale 5, 5225–5240.

Liao, W., Yang, Z., 2022. 3D printing programmable liquid crystal elastomer soft pneumatic actuators. Mater. Horiz. https://doi.org/10.1039/d2mh01001a.

Luo, C., Chung, C., Traugutt, N.A., Yakacki, C.M., Long, K.N., 2021. 3D printing of liquid crystal elastomer foams for enhanced energy dissipation under mechanical insult. ACS Appl. Mater. Interfaces 13, 12698–12708.

Luo, C., Chung, C., Traugutt, N.A., Yakacki, C.M., Long, K.N., Yu, K., 2022a. Real-time alignment and reorientation of polymer chains in liquid crystal elastomers. ACS Appl. Mater. Interfaces 14, 1961–1972.

Luo, C., Chung, C., Yakacki, C.M., Long, K., Yu, K., 2022b. Real-time alignment and reorientation of polymer chains in liquid crystal elastomers. ACS Appl. Mater. Interfaces 14, 1961–1972.

Martin Linares, C.P., Traugutt, N.A., Saed, M.O., Martin Linares, A., Yakacki, C.M., Nguyen, T.D., 2020. The effect of alignment on the rate-dependent behavior of a main-chain liquid crystal elastomer. Soft Matter 16, 8782–8798.

Mistry, D., Traugutt, N.A., Yu, K., Yakacki, C.M., 2021a. Processing and reprocessing liquid crystal elastomer actuators. J. Appl. Phys. 129, 130901.

Mistry, D., Traugutt, N.A., Sanborn, B., Volpe, R.H., Chatham, L.S., Zhou, R., Song, B., Yu, K., Long, K.N., Yakacki, C.M., 2021b. Soft elasticity optimizes dissipation in 3D-printed liquid crystal elastomers. Nat. Commun. 12, 6677.

Nie, X., Song, B., Loeffler, C.M., 2015. A novel splitting-beam laser extensometer technique for Kolsky tension bar experiment. Journal of Dynamic Behavior of Materials 1, 70–74.

Othman, R., Guégan, P., Challita, G., Pasco, F., LeBreton, D., 2009. A modified servo-hydraulic machine for testing at intermediate strain rates. Int. J. Impact Eng. 36, 460–467.

Patil, H.P., Lentz, D.M., Hedden, R.C., 2009. Necking instability during polydomain-monodomain transition in a smectic main-chain elastomer. Macromoledules 42, 3525–3531.

Peng, X., Wu, S., Sun, X., Yue, L., Montgomery, S.M., Demoly, F., Zhou, K., Zhao, R.R., Qi, H.J., 2022. 4D printing of freestanding liquid crystal elastomers via hybrid additive manufacturing. Adv. Mater. 34, 2204890.

Prévôt, M.E., Andro, H., Alexander, S.L.M., Ustunel, S., Zhu, C., Nikolov, Z., Rafferty, S.T., Brannum, M.T., Kinsel, B., Korley, L.T.J., Freeman, E.J., McDonough, J.A., Clements, R.J., Hegmann, E., 2018. Liquid crystal elastomer foams with elastic properties specifically engineered as biodegradable brain tissue scaffolds. Soft Matter 14, 354–360.

Saed, M.O., Torbati, A.H., Nair, D.P., Yakacki, C.M., 2016. Synthesis of programmable main-chain liquid-crystalline elastomers using a two-stage thiol-acrylate reaction. JoVE 107, 53546.

Sharma, A., Mori, T., Mahnen, C.J., Everson, H.R., Leslie, M.T., Nielsen, A.D., Lussier, L., Zhu, C., Malcuit, C., Hegmann, T., McDonough, J.A., Freeman, E.J., Korley, L.T.J., Clements, R.J., Hegmann, E., 2017. Effects of structural variations on the cellular response and mechanical properties of biocompatible, biodegradable, and porous smectic liquid crystal elastomers. Macromol. Biosci. 17, 1600278.

Siddiqui, Z., Smay, J., Azoug, A., 2022. Highly tunable actuation and mechanical properties of 4D-printed nematic liquid crystal elastomers. Mech. Mater. 170, 104329.

Skačej, G., Zannoni, C., 2014. Molecular simulations shed light on supersoft elasticity in polydomain liquid crystal elastomers. Macromolecules 47, 8824–8832.

Song, B., Chen, W., 2004. Loading and unloading SHPB pulse shaping technique for dynamic hysteretic loops. Exp. Mech. 44, 622–627.

Song, B., Martinez, T., Landry, D., Aragon, P., Long, K., 2023. Development of a bench-top intermediate-strain-rate (ISR) test apparatus for soft materials. Journal of Dynamic Behavior of Materials 9, 36–43.

Traugutt, N.A., Mistry, D., Luo, C., Yu, K., Ge, Q., Yakacki, C.M., 2020. Liquid-crystal-elastomer-based dissipative structures by digital light processing 3D printing. Adv. Mater. 32, 2000797.

Ula, S.W., Traugutt, N.A., Volpe, R.H., Patel, R.R., Yu, K., Yakacki, C.M., 2018. Liquid crystal elastomers: an introduction and review of emerging technologies. Liquid Crystal Reviews 6, 78–107.

Volpe, R.H., Mistry, D., Patel, V.V., Patel, R.R., Yakacki, C.M., 2020. Dynamically crystallizing liquid-crystal elastomers for an expandable endplate-conforming interbody fusion cage. Adv. Healthcare Mater. 9, 1901136.

Wang, Y., An, J., Lee, H., 2022a. Recent advances in molecular programming of liquid crystal elastomers with additive manufacturing for 4D printing. Molecular Systems Design & Engineering 7, 1588–1601.

Wang, Z., Boechler, N., Cai, S., 2022b. Anisotropic mechanical behavior of 3D printed liquid crystal elastomer. Addit. Manuf. 52, 102678.

Wang, Z., Guo, Y., Cai, S., Yang, J., 2023. Three-dimensional printing of liquid crystal elastomers and their applications. ACS Appl. Polym. Mater. 4, 3153–3168.

Warner, M., Terentjev, E.M., 2007. Liquid Crystal Elastomers, vol. 120. Oxford university press.

Xiao, X., 2008. Dynamic tensile testing of plastic materials. Polym. Test. 27, 164–178.

Yasuoka, H., Takahashi, K.Z., Fukuda, J., Aoyagi, T., 2021. Molecular architecture dependence of mesogen rotation during uniaxial elongation of liquid crystal elastomers. Polymer 229, 123970.

Zhang, Z., Huo, Y., 2022. Programmable mechanical energy absorption and dissipation of liquid crystal elastomers: modeling and simulations. Adv. Eng. Mater. 24, 2100590.